




Article

The Impact of Diurnal Variability of Sea Surface Temperature on Air–Sea Heat Flux Estimation over the Northwest Pacific Ocean

Qianguang Tu ^{1,2,†}, Zengzhou Hao ^{2,3,†} , Dong Liu ^{4,†}, Bangyi Tao ², Liangliang Shi ¹ and Yunwei Yan ^{5,6,*}

¹ School of Surveying and Municipal Engineering, Zhejiang University of Water Resources and Electric Power, Hangzhou 310018, China; tuqg@zjweu.edu.cn (Q.T.); shill@zjweu.edu.cn (L.S.)

² State Key Laboratory of Satellite Ocean Environment Dynamics, Second Institute of Oceanography, Ministry of Natural Resources, Hangzhou 310012, China; hzyx80@sio.org.cn (Z.H.); taobangyi@sio.org.cn (B.T.)

³ Southern Marine Science and Engineering Guangdong Laboratory (Guangzhou), Guangzhou 511458, China

⁴ Key Laboratory of Watershed Geographic Sciences, Nanjing Institute of Geography and Limnology, Chinese Academy of Sciences, Nanjing 210008, China; dliu@niglas.ac.cn

⁵ Key Laboratory of Marine Hazards Forecasting, Ministry of Natural Resources, Hohai University, Nanjing 210024, China

⁶ Observation and Research Station of Air–Sea Interface, Ministry of Natural Resources, Hohai University, Nanjing 210024, China

* Correspondence: yunwei.yan@hhu.edu.cn

† These authors contributed equally to this work.

Abstract: Accurate and consistent observations of diurnal variability of sea surface temperature (SST DV) and its impact on air–sea heat fluxes over large areas for extended periods are challenging due to their short time scale and wide coverage. The hourly gap-free SSTs generated from Japan Aerospace Exploration Agency–Japan Agency for Marine–Earth Science and Technology (JAXA–JAMSTEC) are input to the COARE3.5 bulk flux algorithm to investigate the impact of SST DV on air–sea heat fluxes over the Northwest Pacific Ocean (NWPO). The main results are as follows. (1) The JAXA–JAMSTEC SSTs were found to be in good agreement with the buoy observations on SST DV with a very slight negative bias of -0.007 °C and a root mean square error of 0.018 °C. (2) The case study conducted on 26 June 2020 showed that the fluxes' diurnal amplitudes were about 30 – 50 $W m^{-2}$, and evolution was in agreement with SST DV. (3) The average impact of SST DV on heat fluxes was 2.93 $W m^{-2}$ over the subtropical NWPO, decreasing from southeast to northwest and from low to high latitudes, and showing a clear seasonal cycle during 2019–2022. This research highlights the need to consider SST DV for accurate estimation of heat fluxes, which is crucial for climate and atmospheric studies.

Keywords: sea surface temperature; diurnal variability; air–sea heat fluxes; Northwest Pacific Ocean; COARE3.5 bulk flux algorithm



Citation: Tu, Q.; Hao, Z.; Liu, D.; Tao, B.; Shi, L.; Yan, Y. The Impact of Diurnal Variability of Sea Surface Temperature on Air–Sea Heat Flux Estimation over the Northwest Pacific Ocean. *Remote Sens.* **2024**, *16*, 628. <https://doi.org/10.3390/rs16040628>

Academic Editor: Martin Gade

Received: 25 December 2023

Revised: 20 January 2024

Accepted: 27 January 2024

Published: 8 February 2024



Copyright: © 2024 by the authors. Licensee MDPI, Basel, Switzerland. This article is an open access article distributed under the terms and conditions of the Creative Commons Attribution (CC BY) license (<https://creativecommons.org/licenses/by/4.0/>).

1. Introduction

Air–sea heat flux is essential for understanding the interaction and energy exchange between the atmosphere and the ocean. It consists of the surface latent heat flux ($qlat$), the sensible heat flux ($qhsb$), as well as shortwave ($qsht$) and longwave radiative fluxes ($qrnl$) [1]. The $qlat$ and $qhsb$ are also referred to as turbulent heat fluxes because both of them are caused by turbulent mixing. Turbulent fluxes can be directly observed using the eddy covariance method. This approach allows the exchange of matter or energy between the atmosphere and the ocean to be measured from research stations or ships. However, direct measurements are usually too difficult and costly. Therefore, parameterization methods are often used to estimate fluxes indirectly. The bulk aerodynamic equations are the most commonly used parameterization method. Turbulent heat fluxes are typically calculated using parameterization schemes based on input variables obtained from buoy observations or satellite-derived products [2]. Sea surface temperature (SST) is one of the most important input variables in these schemes.

During the day, SST is generally minimum in the morning and maximum in the afternoon. The diurnal variation of SST (SST DV) is mainly caused by solar heating and the Earth's rotation, and it has significant impacts on the air–sea interaction [3]. The SST DV is most intense in the first few meters of the surface water column and shows a latitudinal and seasonal dependence. According to the vessel SST measurements in the early and mid-twentieth century, the reported average amplitudes of SST DV range from 0.2 to 0.6 °C [4]. Under calm and clear conditions during daytime, the largest diurnal warming can reach up to 1.5 °C [5]. Since the 1980s, advances in satellite sensors and the development of retrieval algorithms in the field of remote sensing have provided unprecedented opportunities to investigate the spatial and temporal characteristics of SST DV over global or regional oceans. A crucial step in this process is the comparison of satellite-derived SSTs with in situ measurements to ensure the necessary accuracy for the detection of DV [6]. Once validated, satellites provide a unique opportunity to estimate the magnitude and spatial extent of the SST DV over wide regions. Under conditions of light winds and high insolation, the surface diurnal amplitude can reach 3 to 4 °C in the open ocean, and it is not uncommon to observe DV larger than 5 °C in some marginal seas [7–9].

SST DV is essential for estimating air–sea heat exchange [10]. A 1 °C error in SST within the tropical warm pool can lead to an average error of 27 W m^{−2} in the estimation of the net surface heat flux [11]. During the Tropical Ocean Global Atmosphere (TOGA) Coupled Ocean–Atmosphere Response Experiment (COARE), the daytime warm layer increased the net heat flux from the ocean by about 4 W m^{−2} on average [12]. Within the COARE inner intensive flux array, the average diurnal amplitudes of surface latent and sensible heat fluxes were about 35 and 4 W m^{−2}, respectively [13]. Zeng and Dickinson [14] conducted a study of the influence of SST DV on surface fluxes over the tropical Pacific. They found that surface latent and sensible heat fluxes had average diurnal amplitudes of about 19.7 and 5.6 W m^{−2}, respectively. Ward [15] suggested that under calm and clear conditions, the net heat flux from the ocean could increase by 50–60 W m^{−2} in the daytime due to the warm layer effect. Clayson and Bodanoff [16] estimated that neglecting the diurnal SST signal could lead to a globally averaged error in flux calculations of about 4.5 W m^{−2}. On an instantaneous basis, however, the total error can exceed 200 W m^{−2} in tropical areas. Yan et al. [17] recently showed that the SST DV of the warm layer effect causes an increase of 6.0 W m^{−2} in the tropics. Consequently, neglecting SST DV effects can lead to underestimation of air–sea heat fluxes to different extents in different regions.

Accurate observations of SST DV over large areas for extended periods are challenging due to its short time scale and extensive coverage. The current observing system for SST consists mainly of in situ observations from ships (Voluntary Observing Ship and research vessel), buoys (moored and drifting), Argo floats, as well as satellite remote sensing [18]. The in situ measurements or experiments mentioned above were typically of short duration and relatively sparse in space. Satellite data can provide regular sampling and extensive area coverage [19]. However, there may be significant gaps within a single satellite-derived SST due to the presence of clouds or dense aerosol layers. Various numerical or empirical models have been used to obtain global gap-free SST for heat flux calculations. It should be noted that no model can perfectly simulate the diurnal variations [20]. The accuracy of the evaluation of heat flux DV can be reduced by the large uncertainty of the model SST DV. An alternative approach is to use SST assimilated from multiple sources, including satellites and SST models. The assimilated SST typically provides better accuracy, higher spatio-temporal resolution, and full coverage [21].

The aim of this study is to evaluate the impact of SST DV on the estimation of air–sea heat fluxes over the Northwest Pacific Ocean (NWPO). First, we validate a four-year dataset of high-resolution hourly SST assimilated from multiple sources, including a geostationary satellite. The assimilated SST is then used, along with other reanalysis data, as input to the COARE3.5 bulk algorithm to calculate air–sea heat fluxes. To investigate the impact of SST DV on air–sea heat fluxes, the study calculates the difference between two scenarios: one with and one without SST DV within the COARE3.5 framework. Section 2 provides

details on data and methodology. The results are summarized in Section 3, followed by discussions in Section 4. The conclusions of the study are presented in Section 5.

2. Materials and Methods

2.1. Study Area

The research area is located on the NWPO and extends from 117°E to 150°E and 17°N to 50°N, as shown in Figure 1. The domain includes extensive ocean areas, numerous islands, and a diverse coastline. The geographic diversity of the region creates a dynamic and complex environment. The climate of the NWPO exhibits a wide range, transitioning from tropical to subtropical and temperate. This climatic variability is significantly influenced by the interaction between the East Asian monsoon and oceanic circulation patterns. The NWPO experiences distinct seasonal shifts during the summer monsoon (July to August), characterized by a weak southwesterly flow, and the winter months (September to April of the following year), characterized by strong northeasterly winds. Major ocean currents, such as the Kuroshio, play a crucial role in shaping both the oceanic and atmospheric conditions in the NWPO [22]. This dynamic interplay of oceanic currents contributes to the uniqueness of the region's environment. The NWPO is susceptible to typhoons and tropical storms, adding to the complexity of its natural environment. These extreme weather events have a significant impact on the region's atmospheric and oceanic dynamics. To provide a detailed assessment, we selected six distinct areas of interest within the domain based on their physical geographic characteristics. These areas are shown in Figure 1 and detailed in Table 1. They include the Bohai and Yellow Sea (BYS), the Japan Sea (JPS), the East of Japan (EOJ), the East China Sea (ECS), the South of Japan (SOJ), and the subtropical Northwest Pacific (SNWP).

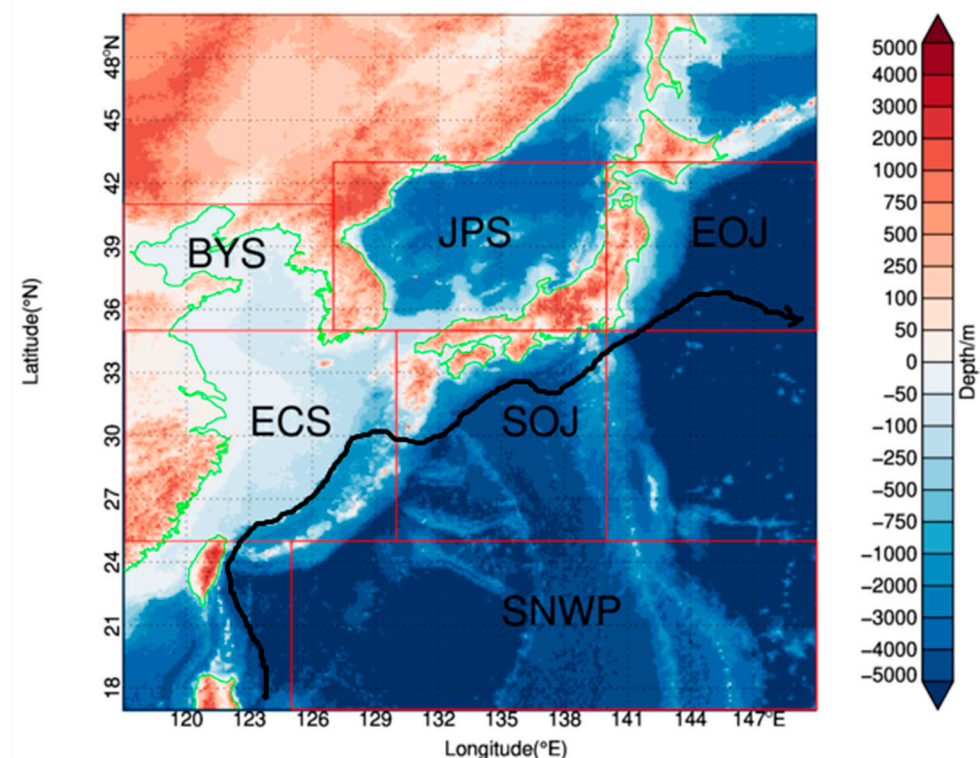


Figure 1. Topography of the study domain and six areas of interest: the Bohai and the Yellow Sea (BYS), the Japan Sea (JPS), East of Japan (EOJ), East China Sea (ECS), South of Japan (SOJ), and the subtropical Northwestern Pacific (SNWP). The green lines illustrate the shoreline. The black curve with arrow indicates the major ocean current of Kuroshio and its extension. Note that the color bar of the depth scale are nonlinear.

Table 1. Summary of the six distinct areas in the Northwestern Pacific for detailed evaluation.

Domain	Location	Longitude (°E)	Latitude (°N)	Characteristics
BYS	the Bohai and the Yellow Sea	117–127	35–41	semi-enclosed sea with relatively shallow water
JPS	Japan Sea	127–140	35–43	a marginal sea with a relatively narrow continental shelf and deep basin
EOJ	East of Japan	140–150	35–43	influenced by the Kuroshio Extension
ECS	East China Sea	117–130	25–35	encompasses a diverse range of coastal features, islands, ocean currents, and ecosystems
SOJ	South of Japan	130–140	25–35	Influenced by the East Asian monsoon, typhoons, and Kuroshio Current
SNWP	subtropical Northwestern Pacific	125–150	17–25	hot summers and warm winters

2.2. Multi-Source SST

Hourly SST from JAXA-JAMSTEC (Japan Aerospace Exploration Agency–Japan Agency for Marine–Earth Science and Technology) and other atmospheric variables from ERA5 (Fifth generation of ECMWF Atmospheric Reanalysis of the Global Climate) are used to estimate air–sea heat fluxes over the NWPO during 2019–2022. The atmospheric variables include 10 m wind speed, 2 m air temperature, 2 m dew point temperature, sea level pressure, solar shortwave radiation, and longwave incident radiation. These inputs are used to run the COARE 3.5 algorithms.

The JAXA-JAMSTEC SST is generated from six types of satellite-derived SST and one model SST. The satellite-derived SST datasets were provided by JAXA, including three infrared SSTs and three microwave SSTs, as listed in Table 2. The algorithm of the infrared SST products is developed by [23,24] and the algorithm of the microwave SST products is based on [25]. The infrared SST has a fine spatial resolution of about 250 m to 2 km but is limited by its inability to penetrate clouds. Microwave SST, on the other hand, has a coarse spatial resolution of approximately 25 km, but can penetrate clouds, rain, and snow in all weather conditions.

Table 2. Multi-source satellite SST data used.

Satellite	Sensor	Orbit	Bands	Spatial Resolution	Temporal Resolution
Himawari-8	AHI	geostationary	infrared	2 km	10 min
GCOM-C	SGLI	sun-synchronous	infrared	250 m–1 km	twice per day
Suomi NPP	VIIRS	sun-synchronous	infrared	750 m	twice per day
GCOM-W	AMSR2	sun-synchronous	microwave	25 km	twice per day
GPM-Core	GMI	non-sun-synchronous	microwave	25 km	twice per day
Coriolis	Windsat	sun-synchronous	microwave	25 km	twice per day

Note: Himawari-8 is a Geostationary Meteorological Satellite, Advanced Himawari Imager (AHI); the Global Change observation Mission–Climate satellite (GCOM-C), Second-Generation Global Imager (SGLI), the Suomi National Polar-orbiting Partnership satellite (Suomi NPP), Visible Infrared Imaging Radiometer Suite (VIIRS); Global Change Observation Mission–Water satellite (GCOM-W), Advanced Microwave Scanning Radiometer 2 (AMSR2); Global Precipitation Measurement (GPM) Core Observatory, Microwave Imager (GMI); WindSat on board the Coriolis satellite.

The model SST used in the assimilation is derived from the high-resolution regional ocean model “JCOPE-T (Japan Coastal Ocean Predictability Experiment)”, developed by the Japan Agency for Marine–Earth Science and Technology (JAMSTEC). The JCOPE-T model provides hourly ocean state variables, including sea level, temperature, salinity, and current velocity, within the study area. The model has a spatial resolution of $1/36^\circ$ and a vertical resolution of 46 layers. The top surface layer is located at a depth of 0 m. To better

capture high-frequency changes and small-scale processes within the study area, a multi-scale three-dimensional variational method was employed [26]. The above-mentioned satellite-derived SST data are included in the model. Since the Himawari-8 infrared SST is the main source for the hourly JAXA-JAMSTEC SST generation, we assume here that the SST product has the diurnal variability of the skin SST. To be consistent with the spatial resolution of other reanalysis data and to reduce noise, the JAXA-JAMSTEC SST was resampled from $1/36^\circ$ to $1/4^\circ$ using bilinear interpolation.

ERA5 (Fifth generation of ECMWF Atmospheric Reanalysis of the Global Climate) is an atmospheric reanalysis dataset developed by the European Centre for Medium-Range Weather Forecasts (ECMWF) [27]. It provides high-resolution global meteorological and climatic data by integrating the latest meteorological observations, satellite data, ground station observations, and advanced numerical weather prediction models through data assimilation techniques. ERA5 produces continuous and consistent global atmospheric, land and ocean state data by reanalyzing historical meteorological observations. The ERA5 dataset spans from 1940 to the present and provides high spatial ($0.25^\circ \times 0.25^\circ$) and temporal (1 h) resolution. It serves as a valuable resource for climate research. The study uses hourly DV field data, including wind speed at 10 m, air temperature at 2 m, and dew point temperature at 2 m, sea level pressure, solar shortwave radiation, and longwave incident radiation. Although ERA5 provides hourly skin SST, it is a relatively recent reanalysis and many formal validation reports over the domain have not been published.

To evaluate the accuracy of the hourly SST from ERA5 and JAXA-JAMSTEC, the in situ SST observations from the Kuroshio Extension Observation (KEO) surface mooring were used. KEO is the only site of the Ocean Climate Stations Project (OCS) [28] in the study area. The mission of the OCS is to record meteorological and oceanographic measurements from autonomous platforms. These reference time series and innovative measurements are used to improve satellite products, forecast models, and understanding of air–sea interactions and their role in the climate system. During the study period, the KEO buoy was deployed sequentially in three missions (KE-016, -017, and -018). The anchor position changed with each deployment but remained within 25 km of the nominal location (32.3°N , 144.6°E). The KEO buoy measures the top layer temperature at a depth of about 1.2 m below the ocean surface. It also measures wind speed, air and sea temperature, specific humidity, and other meteorological and oceanographic variables at 10 min averages. These variables are necessary to calculate the warm layer and cool skin effects and adjust the 1.2 m KEO measurement layer for ERA5 and JAXA-JAMSTEC SST evaluation.

2.3. Heat Flux Calculation

The impact of SST DV on heat fluxes is determined by calculating the difference between air–sea heat fluxes with and without consideration of SST DV. The calculation includes only $qlat$, $qhsb$, and $qrnl$, as $qsht$ remains constant in both scenarios. The COARE algorithm, which is based on the bulk aerodynamic equation, has been widely used to calculate turbulent fluxes at the sea surface [29,30]. Twelve bulk algorithms were evaluated, and COARE was found to be one of the most accurate algorithms [31]. In this study, we used the latest version of COARE 3.5, released in 2013 [32], to calculate the turbulent fluxes. We input the hourly JAXA-JAMSTEC SST into the algorithm as diurnal SST fields. For non-diurnal SST fields, we used hourly SST data obtained by linear interpolation of predawn SST values from two consecutive days. Predawn SST is defined as the mean temperatures between 0:00 and 4:00 local solar time (LST), according to [7]. The other variables used in COARE 3.5 for heat flux calculations remain the same in both scenarios. The equations are as follows:

$$qhsb = \rho_a C_{pa} C_h (T_s - \theta) u_{10} \quad (1)$$

$$qlat = \rho_a L_e C_e (q_s - q_a) u_{10} \quad (2)$$

$$qrnl = \varepsilon (\sigma (T_s + 273.15)^4 - R_l) \quad (3)$$

where ρ_a represents the air density (in kg m^{-3}); C_{p_a} is the specific heat capacity of air at constant pressure (in J kg^{-1}); L_e represents the latent heat of water vapor evaporation (in J kg^{-1}); C_h and C_e are the coefficients of sensible heat exchange and latent heat exchange, respectively; T_s refers to sea surface temperature (in $^{\circ}\text{C}$), while θ represents the air temperature at the near-surface layer (in $^{\circ}\text{C}$); u_{10} is wind speed at 10 m (in m s^{-1}); q_s and q_a is the surface water vapor specific humidity and surface air specific humidity (in g kg^{-1}), respectively; ε is the emissivity of seawater, generally assumed to be 0.984. The Stefan–Boltzmann constant, denoted by σ , is generally taken as $5.67 \times 10^{-8} (\text{J s}^{-1} \text{m}^{-2} \text{K}^{-4})$. In formula (2), q_s is calculated from the saturated specific humidity of pure water at a temperature of T_s , while q_a is calculated from the saturated specific humidity of air at a temperature of T_a , relative humidity, and sea surface temperature. These values are calculated by the following equations:

$$q_s = 0.98q_{sat}(T_s) \quad (4)$$

$$q_a = RHq_{sat}(T_a) \quad (5)$$

where q_{sat} is the saturation relative humidity, which refers to the relative humidity of the saturated moist air at a certain temperature and pressure. (4) The constant 0.98 in the formula takes into account the presence of salt in seawater, which reduces the number of water molecules on the sea surface, resulting in a 2% decrease in the saturation relative humidity; RH represents the relative humidity of the air. The formula for calculating the air temperature θ near the sea surface is as follows:

$$\theta = T_a + 0.0098z_r \quad (6)$$

where T_a is the air temperature at z_r . In this study, 2 m air temperature from ERA5 is used, so it is equal to 2 here.

3. Results

3.1. Comparison of SST DV

The KEO mooring buoy, which is equipped with high-frequency observing capabilities, was used as a reference to evaluate the SST DV provided by ERA5 and JAXA-JAMSTEC. The spatiotemporal matching window for the mooring buoy and ERA5 and JAXA-JAMSTEC SST was within ± 0.5 h and 1 pixel (25 km). Throughout the study period, there were approximately 737 days and 17,688 sets of effectively matched samples for comparison. The SST DV bias for JAXA-JAMSTEC was -0.007 $^{\circ}\text{C}$ on average, indicating a very slight negative bias, with a root mean square error (RMSE) of 0.018 $^{\circ}\text{C}$. For ERA5, the overall average bias of SST DV was -0.04 $^{\circ}\text{C}$, also with a negative bias, and a larger RMSE of 0.086 $^{\circ}\text{C}$ compared to JAXA-JAMSTEC. Figure 2 depicts the average SST DV for boreal winter (DJF), spring (MAM), summer (JJA), and autumn (SON), respectively. The figure shows KEO as black dots, ERA5 as a dashed line, and JAXA-JAMSTEC as a solid line. According to the observations from the KEO mooring buoy, the SST experiences a weak cooling during the nighttime from 00:00 to 06:00 LST. The largest nocturnal cooling amplitude of about 0.1 $^{\circ}\text{C}$ is observed in summer, followed by spring and autumn, and almost disappears in winter. The temperature begins to rise at 07:00 LST, reaching its peak around 15:00 LST, and then gradually cooling down. The SST DV exhibits the largest amplitude during summer, followed by spring and autumn, and is smallest in winter. Specifically, the average amplitude of DV is close to 0.5 $^{\circ}\text{C}$ in summer, about 0.3 $^{\circ}\text{C}$ in spring, less than 0.2 $^{\circ}\text{C}$ in autumn, and almost negligible in winter, at only 0.03 $^{\circ}\text{C}$.

It is noteworthy that the temperature at the end of each diurnal cycle in spring and summer can be slightly higher, by about 0.02 – 0.04 $^{\circ}\text{C}$, than at the beginning of each diurnal cycle. This difference gradually decreases or disappears in autumn and winter. This phenomenon is mainly due to the continuous increase in SST from spring to summer, reaching a maximum in summer, followed by a cooling trend in autumn and reaching the coldest point in winter. For ERA5, the peak of diurnal warming generally occurs at 13:00–14:00 LST. The amplitude of diurnal warming in summer and spring is significantly

lower by about $0.15\text{ }^{\circ}\text{C}$, and there is a rapid cooling rate in the afternoon. In contrast, JAXA-JAMSTEC SST shows excellent agreement with KEO observations for SST DV. Therefore, JAXA-JAMSTEC SST was selected for further calculations and analysis of air–sea heat fluxes' DV instead of ERA5 SST.

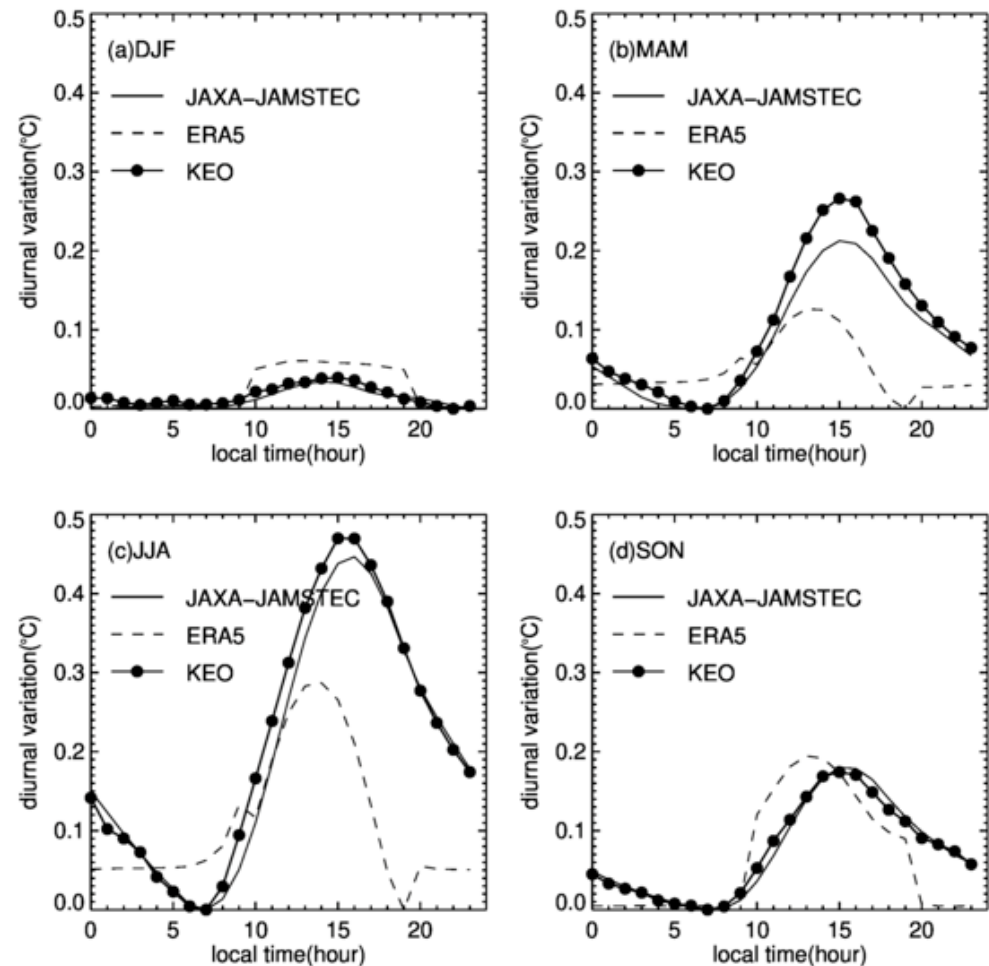


Figure 2. Comparison of the SST DV for KEO mooring observations against ERA5 and JAXA-JAMSTEC: (a) winter (DJF), (b) spring (MAM), (c) summer (JJA), and (d) autumn (SON).

3.2. Diurnal Variation in the Instantaneous Flux over the NWPO

Figure 3 presents SST DV maps for 26 June 2020, capturing the entire diurnal variation from 00:00 to 24:00 LST from JAXA-JAMSTEC SST. During the nighttime, from 00:00 to dawn, the sea surface experiences heat loss, resulting in a continuous decrease in surface temperature. As the sun rises, the sea surface cools in the early morning until solar shortwave radiation exceeds the heat loss. A significant warming trend occurs from 8:00 to 9:00 LST, reaching its peak at 15:00–16:00 LST. The rate of warming then slows, leaving a residual warm layer.

The spatial and temporal distributions of SST DV show significant variability dictated by local conditions, resulting in the emergence of two distinct large-scale warming regions. One region is located north of 30°N east of the China Seas and includes the Yellow Sea and the northern ECS. It has a warming amplitude of up to $1.5\text{ }^{\circ}\text{C}$. The other is in the subtropics of the NWPO, between $18\text{--}30^{\circ}\text{N}$ and $126\text{--}150^{\circ}\text{E}$, with a maximum warming amplitude of $1.5\text{ }^{\circ}\text{C}$. In particular, the maximum warming is observed near 26°N and gradually decreases towards the north and south. In addition, there is a diurnal warming effect of about $1.0\text{ }^{\circ}\text{C}$ in the western part of the Japan Sea. These effects are demonstrated by a pattern of cooling during the nighttime and early morning, warming during the day, and a residual warm

layer afterwards. This pattern highlights the complex dynamics of SST throughout the diurnal cycle.

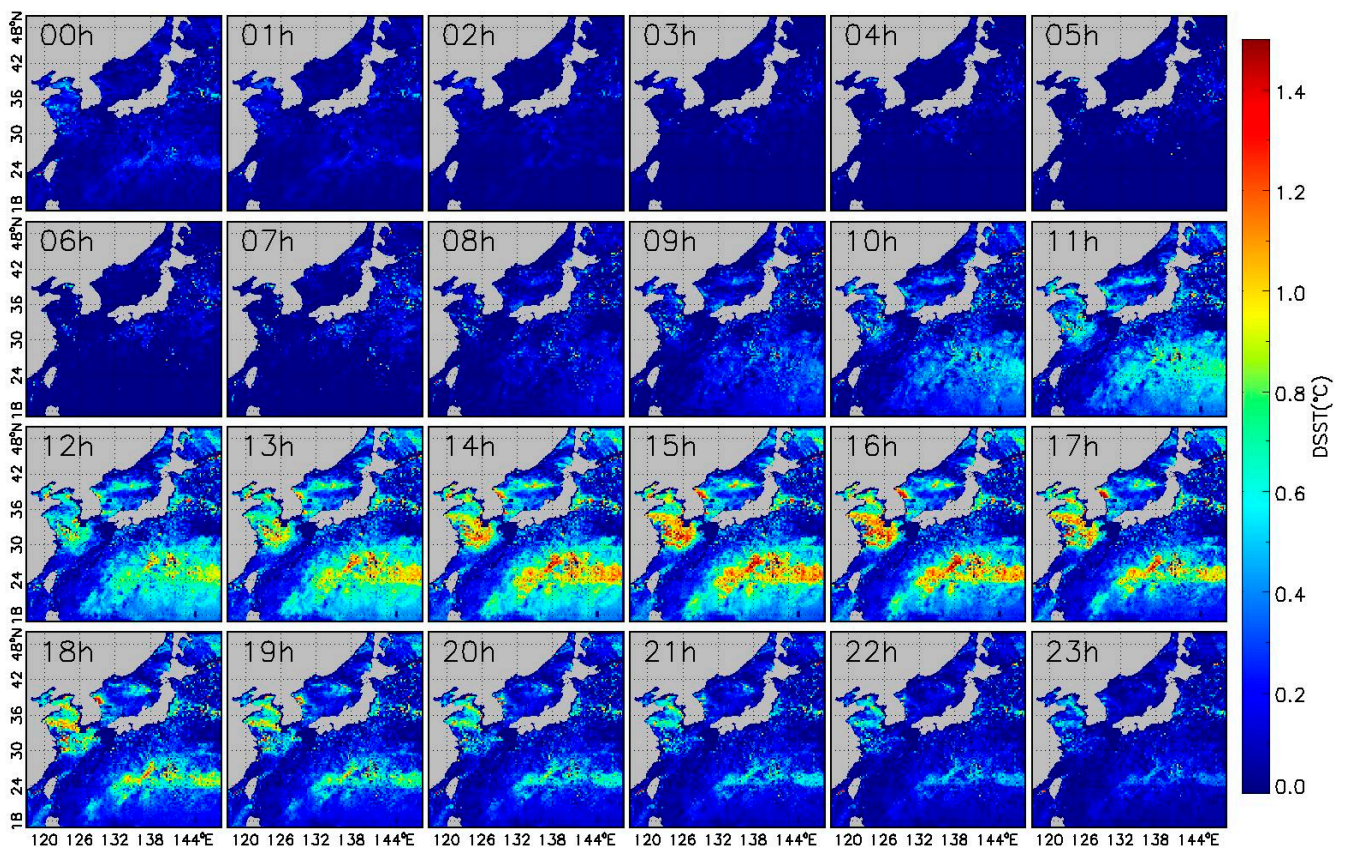


Figure 3. The images of SST DV from 00:00 to 24:00 LST on 26 June 2020. SST DV is estimated by calculating the difference between hourly SST and predawn SST (the average temperatures between 0:00 and 4:00 LST).

Figure 4 shows the hourly evolution of the difference in net heat flux with and without considering the SST DV for 26 June 2020. The differences in the flux fields closely follow the SST DV pattern shown in Figure 3. There are no discernible differences in regions where the sun is below the horizon. However, in sunlit areas, low SST DV is often attributed to factors such as cloud cover, low insolation, or relatively strong winds. We find that this corresponds to a comparatively small difference in net heat flux. Significant differences of about $30\text{--}50\text{ W m}^{-2}$ in net heat fluxes are observed over the ECS and SNWP in the early afternoon. This temporal window corresponds to instances where diurnal warming exceeds $1\text{ }^{\circ}\text{C}$. In these scenarios, the instantaneous error in the sensible heat flux exceeds 6 W m^{-2} , which is up to 130% of the non-diurnal sensible heat flux. The overall error range of the latent heat flux is even more pronounced, with local differences reaching 24 W m^{-2} or more, which exceeds 40% of the non-diurnal latent heat flux. In comparison, the longwave radiation flux differences, which typically hover around 7 W m^{-2} , are of similar magnitude to the sensible heat flux differences. However, the longwave radiation differences account for a smaller percentage of the non-diurnal longwave radiation flux, about 12%. This analysis highlights the importance of accounting for SST DV. Neglecting these variations can introduce a systematic bias in daily heat flux estimates, which may affect the accuracy and reliability of broader climate and atmospheric studies.

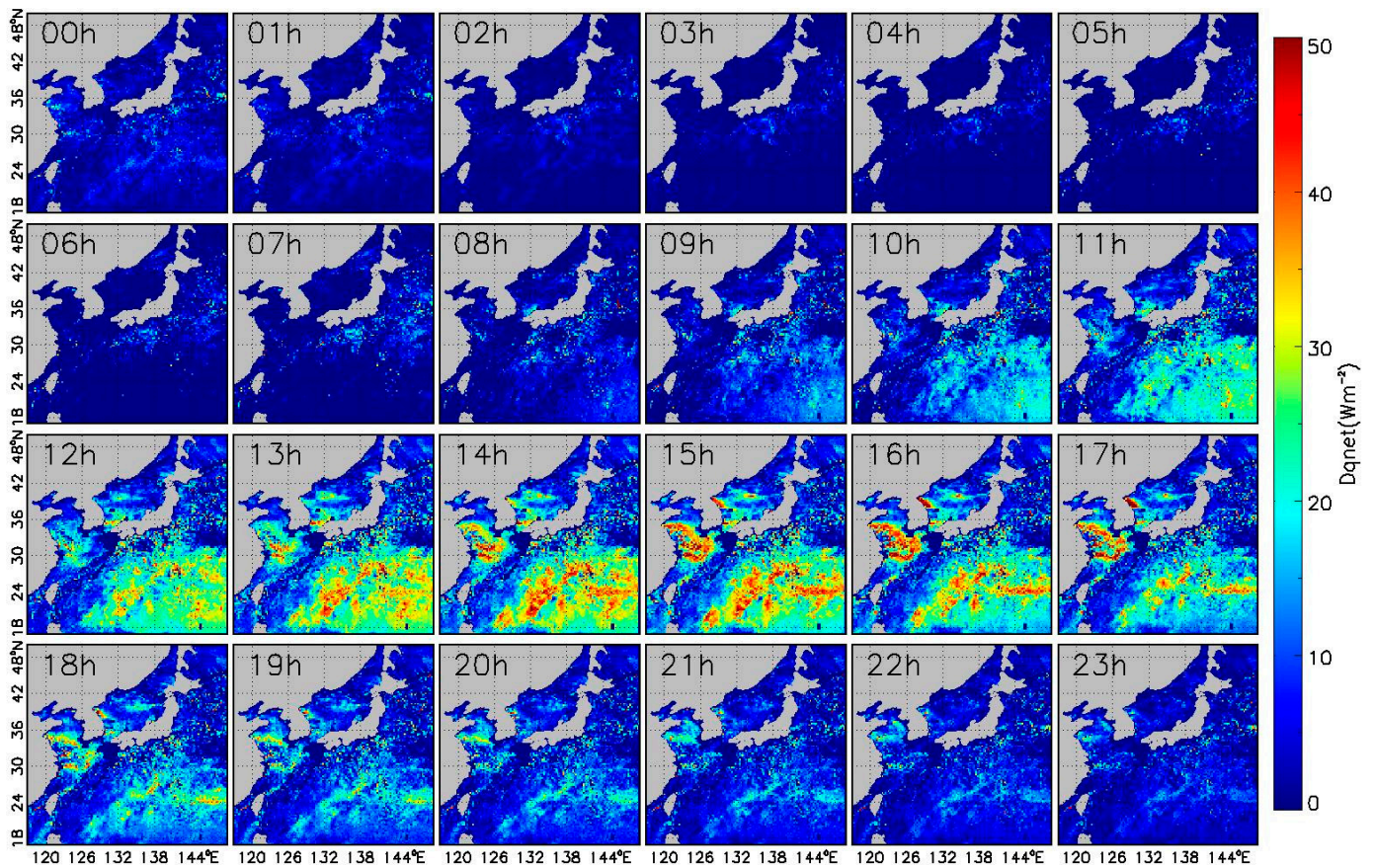


Figure 4. The hourly evolution of the difference in net heat flux with and without considering the SST DV for 26 June 2020.

3.3. Spatial and Temporal Variation Characteristics

3.3.1. Spatial Characteristics

Figure 5 presents a spatial distribution of the average differences resulting from heat flux, including and excluding the SST DV in the heat flux calculations from 2019 to 2022. The differences in latent heat flux (D_{qlat}) decrease from southeast to northwest and from low to high latitudes. The large D_{qlat} values are mainly found in the SNWP and reach about 2.93 W m^{-2} (as listed in Table 3). The differences in sensible heat flux (D_{qhsb}) follow a similar pattern to D_{qlat} , with a spatial correlation coefficient of 0.95. The average D_{qhsb} in the SNWP is approximately 0.74 W m^{-2} . The net longwave radiation differences (D_{qrnl}) have an amplitude close to D_{qhsb} , with e values in the SNWP and small values over the Kuroshio. The differences in total net heat flux (D_{qnet}) show good agreement with D_{qlat} , where D_{qlat} accounts for about 50–70% of D_{qnet} .

Table 3 also lists the maximum differences in heat fluxes for sub-areas using diurnal and non-diurnal SST. The maximum differences for the whole domain are quantified to be about 93.6 W m^{-2} . It is worth noting that significant differences are found between the different sub-regions, as both the SST DV and the wind regime play a role. The largest differences, reaching 192.9 W m^{-2} , are clearly manifested in the EOJ. In contrast, the SNWP shows the least variation among the sub-regions studied.

Figure 6 presents detailed histograms and cumulative probabilities (indicated by the red line) that demonstrate the differences between diurnal and non-diurnal SST variability in the calculation of heat flux components (in columns) in six distinct areas (in rows). Very few negative D_{qnet} values are observed in the BYS, ECS, and EOJ, indicating that the ocean is absorbing heat from the atmosphere. In other areas, D_{qnet} is positive. The positive D_{qnet} ranges from 0 to 6 W m^{-2} , with over 20% of cases exceeding 4 W m^{-2} . This highlights

the significant influence of SST DV on the magnitudes of heat fluxes and emphasizes the importance of careful consideration of SST DV in oceanographic models. D_{qlat} is mainly distributed between 0 and 4 W m^{-2} and accounts for the majority of D_{qnet} . The BYS, ECS, and JPS regions experience a peak position around 1 W m^{-2} , while in the SOJ and SNWP, this peak reaches higher thresholds of 1.5 and 3 W m^{-2} , respectively. In contrast, D_{qhsb} is relatively small, mainly distributed between 0 and 1 W m^{-2} . In general, the differences in magnitude are smaller at higher latitudes than at lower latitudes. The histogram of D_{qrnl} is similar to that of D_{qhsb} , but with a smaller amplitude range from 0 to 0.8 W m^{-2} .

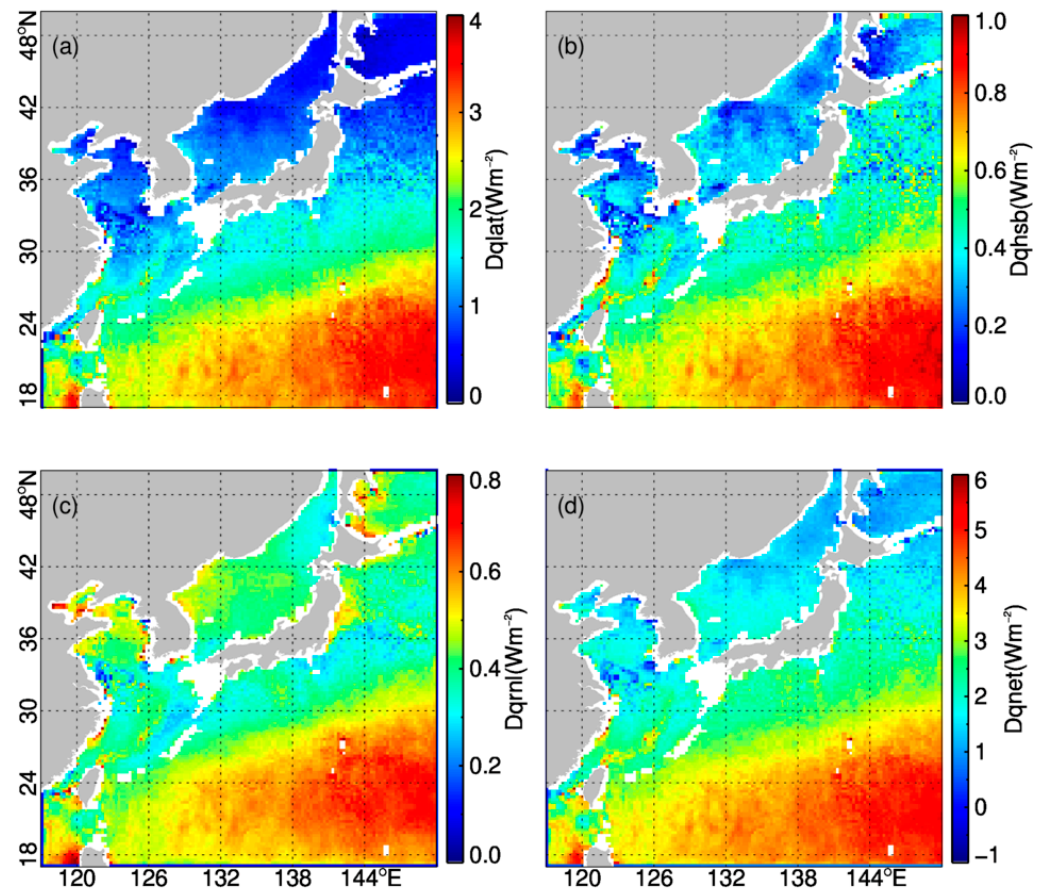


Figure 5. The spatial distribution of the difference when considering and not considering the SST DV in the calculation of heat fluxes for the period 2019–2022: (a) latent heat flux difference, (b) sensible heat flux difference, (c) net longwave radiation difference, and (d) net heat flux difference.

Table 3. Statistics of the difference between the inclusion and exclusion of the SST DV in the calculation of heat fluxes for the study period.

Area	$D_{qlat} (\text{W m}^{-2})$		$D_{qhsb} (\text{W m}^{-2})$		$D_{qrnl} (\text{W m}^{-2})$		$D_{qnet} (\text{W m}^{-2})$	
	Mean	Max	Mean	Max	Mean	Max	Mean	Max
BYS	0.91	62.8	0.24	26.1	0.47	10.4	1.6	94.4
JPS	1.02	56.6	0.33	27.7	0.42	9.9	1.77	87.8
ECS	1.07	70.9	0.40	25.2	0.37	10.3	1.84	102.7
SOJ	1.43	66.4	0.41	21.7	0.37	10.0	2.22	94.1
EOJ	1.85	111.1	0.50	70.1	0.42	19.4	2.78	192.9
SNWP	2.93	51.7	0.74	14.5	0.58	8.2	4.27	72.2
ALL	1.86	61.8	0.52	25.4	0.46	10.3	2.83	93.6

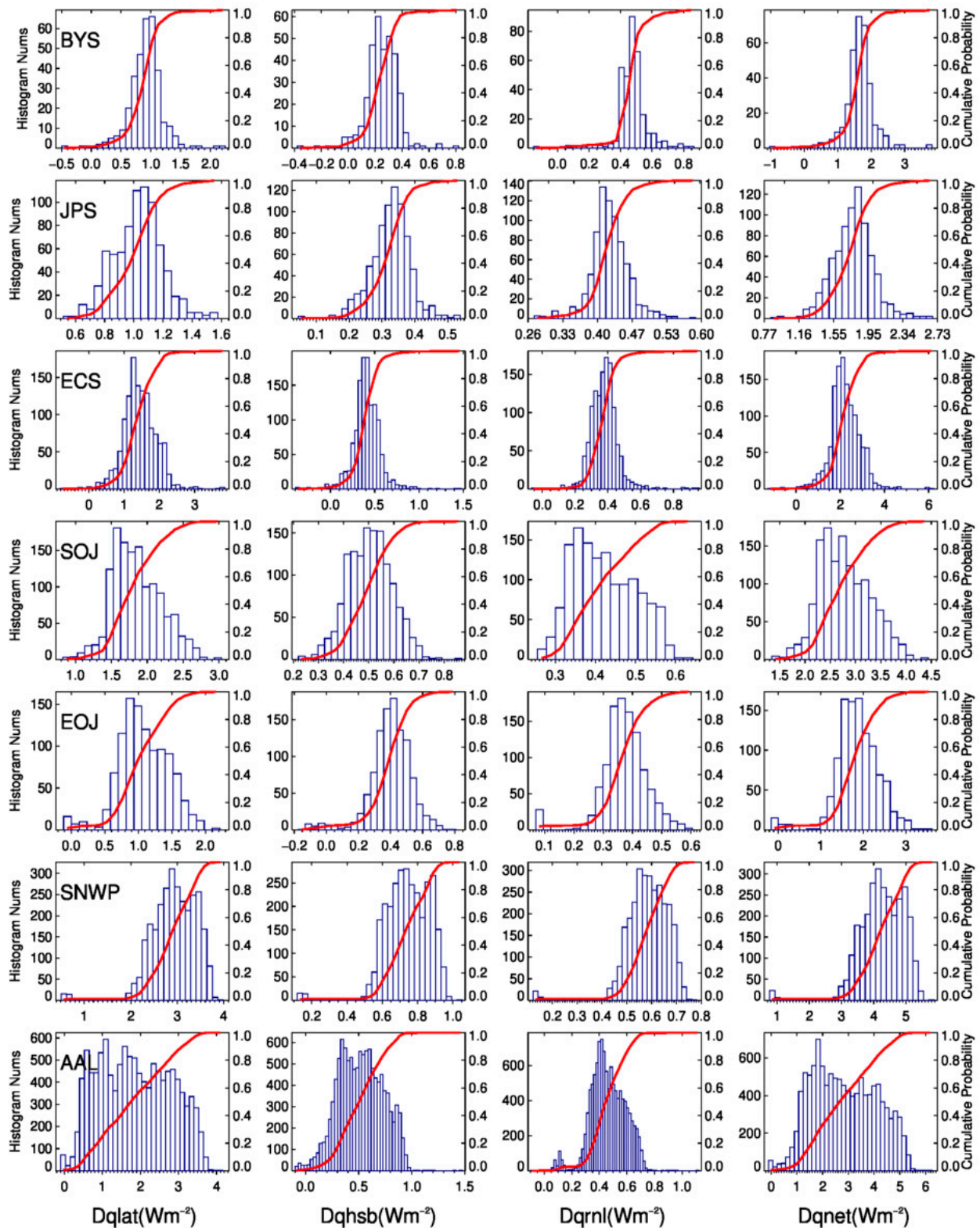


Figure 6. Histogram and cumulative probability (red line) of the difference between the estimation of heat flux that include and exclude the SST DV (in columns) at different areas (in rows) for the period 2019–2022.

3.3.2. Seasonal Variation

Figure 7 displays the seasonal variations in the heat flux difference resulting from the inclusion and exclusion of the SST DV in the calculation of the heat fluxes for the period 2019–2022. The largest discrepancies in the net heat flux and its components throughout

the entire domain occur in the region influenced by the subtropical high-pressure system, between 24–30°N and 140–150°E, reaching values above 8 W m^{-2} in summer. In the SNWP region, the largest differences are observed in spring, followed by summer, with winter exhibiting the smallest variations. The average differences in net heat flux in spring can reach $6\text{--}8 \text{ W m}^{-2}$. In the ECS region, the differences in heat flux are most pronounced in summer, followed by spring, with winter slightly exceeding autumn, especially in the Kuroshio Current region. The seasonal variation patterns of the net heat flux and its components in the other four areas (BYS, JPS, EOJ, and SOJ) are similar. The values are highest in summer, followed by spring, autumn, and winter, although the intensities vary slightly among the sub-regions; apart from summer, the differences in net heat flux and its components in the SNWP region tend to be larger than those in other regions during the same season. A possible explanation is that the sun's rays shine directly over the areas south of the NWPO in spring, autumn, and winter, so the incident shortwave radiation gradually increases from north to south in a large difference in SST DV and net heat flux SNWP.

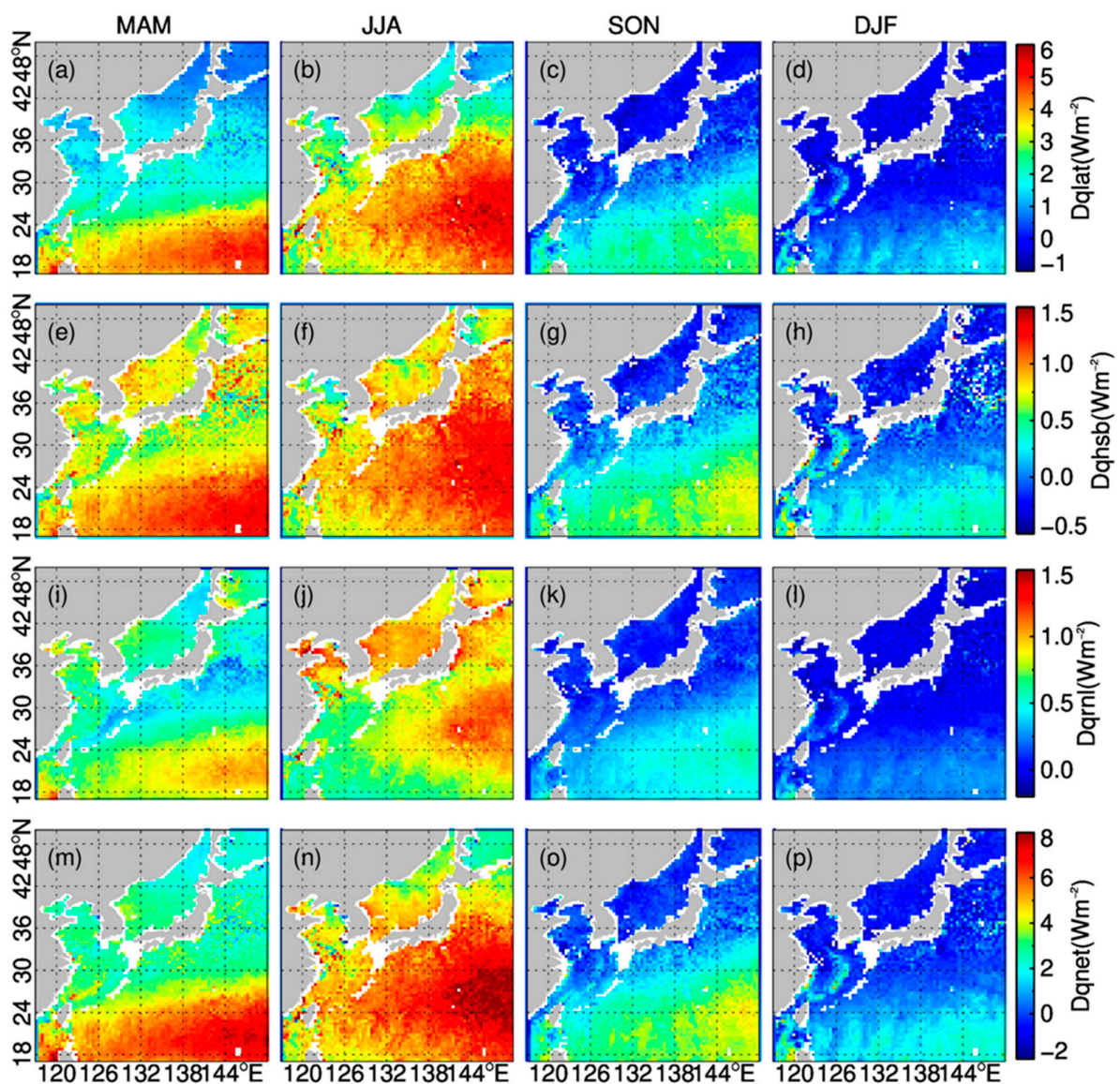


Figure 7. Seasonal variations of the difference between the inclusion and exclusion of the SST DV in the calculation of heat fluxes for the period 2019–2022, (a–d) latent heat flux difference, (e–h) sensible heat flux difference, (i–l) net long-wave radiation difference and (m–p) net heat flux difference. MAM (March–April–May), JJA (June–July–August), SON (September–October–November), and DJF (December–January–February).

Figure 8 illustrates the time series of hourly and daily mean differences resulting from the inclusion and exclusion of the SST DV in the heat flux calculations for the study domain during the period 2019–2022. It is evident that the differences in heat flux are dominated by a seasonal cycle, peaking in the summer months. Most of the large hourly (instantaneous) net heat flux differences exceeding 10 W m^{-2} are prevalent in the spring and summer. During the summer period, there are many daily mean net heat flux differences exceeding 4 W m^{-2} . In order to identify patterns and trends, a 45-day running mean is applied to the daily mean, shown by the red line. This smoothing technique is particularly helpful in the presence of the pronounced seasonal cycle.

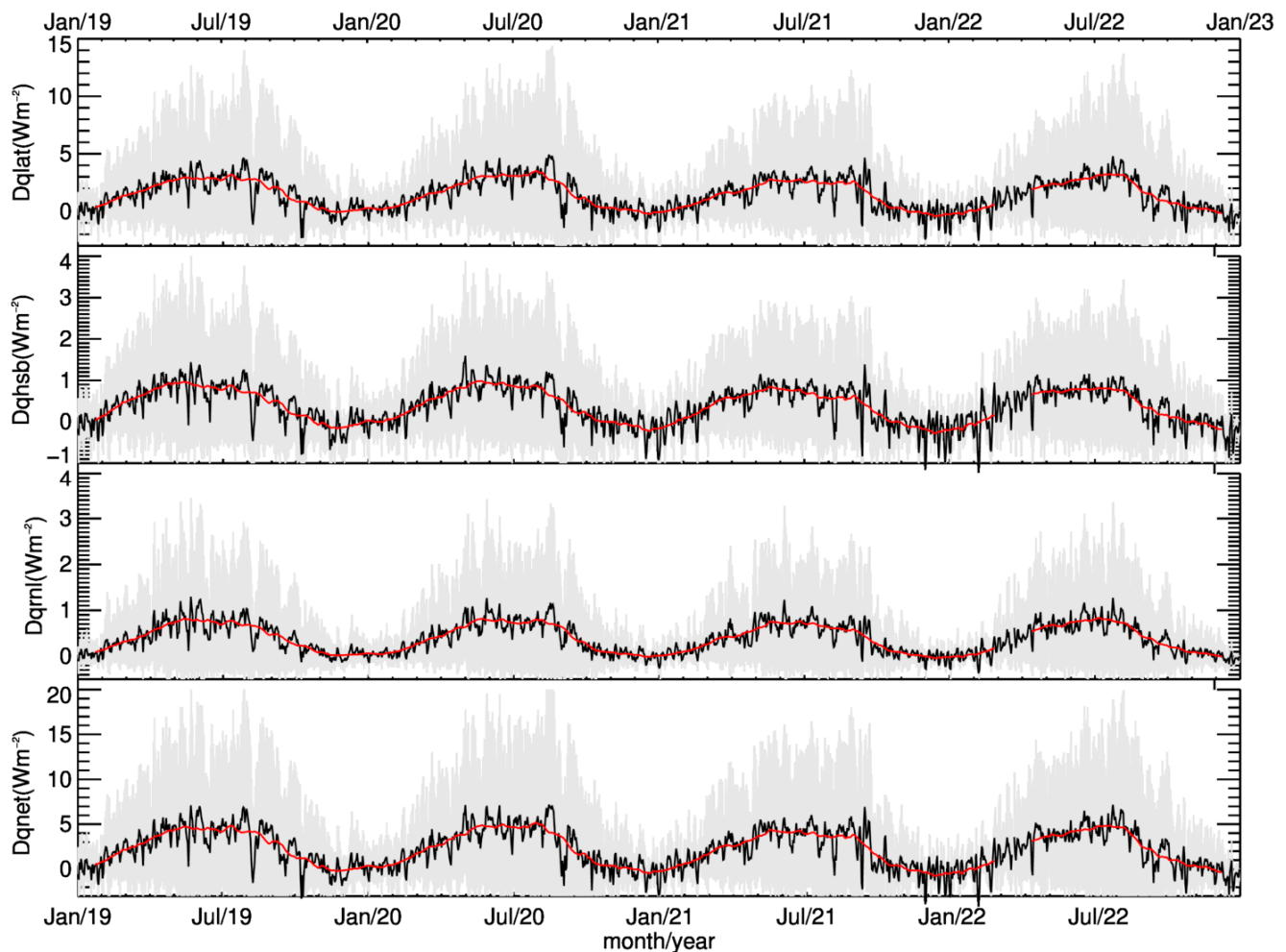


Figure 8. The time series of the hourly (gray line) and daily mean (black line) differences between the inclusion and exclusion of the SST DV in the calculation of heat fluxes for the period 2019–2022 in the domain. The red line represents a fit to a 45-day running mean.

4. Discussion

4.1. The Factors Influencing SST DV

The SST DV is a complex phenomenon influenced by various factors, such as solar radiation, sea surface winds, clouds, precipitation, dynamic ocean processes, and biological processes [9,33,34]. In particular, solar radiation is the primary driver of SST DV, causing the upper ocean to absorb a significant amount of heat, resulting in a positive correlation with SST DV. Sea surface wind speed induces oceanic mixing and takes heat from the ocean to the atmosphere, exhibiting a significant negative correlation with SST DV.

This relationship is confirmed by the seasonal variation in the spatial distribution, as shown in Figure 9. For example, in the Kuroshio region (black line in Figure 1) during

spring (MAM) and summer (JJA), where the average wind speed is about 7 ms^{-1} , the SST DV of approximately $0.05\text{--}0.1 \text{ }^\circ\text{C}$ in spring is significantly smaller than that of about $0.1\text{--}0.15 \text{ }^\circ\text{C}$ in summer. This difference is primarily due to the stronger solar radiation in this region in summer, which is about 50 Wm^{-2} higher than in spring. In the study domain, the summer season is characterized by strong solar radiation. The SST DV reaches its maximum value for the entire year. The maximum values of SNWP occur in spring. In winter, diurnal warming decreases in the region north of 30 degrees in the study area due to weak solar radiation and strong winds.

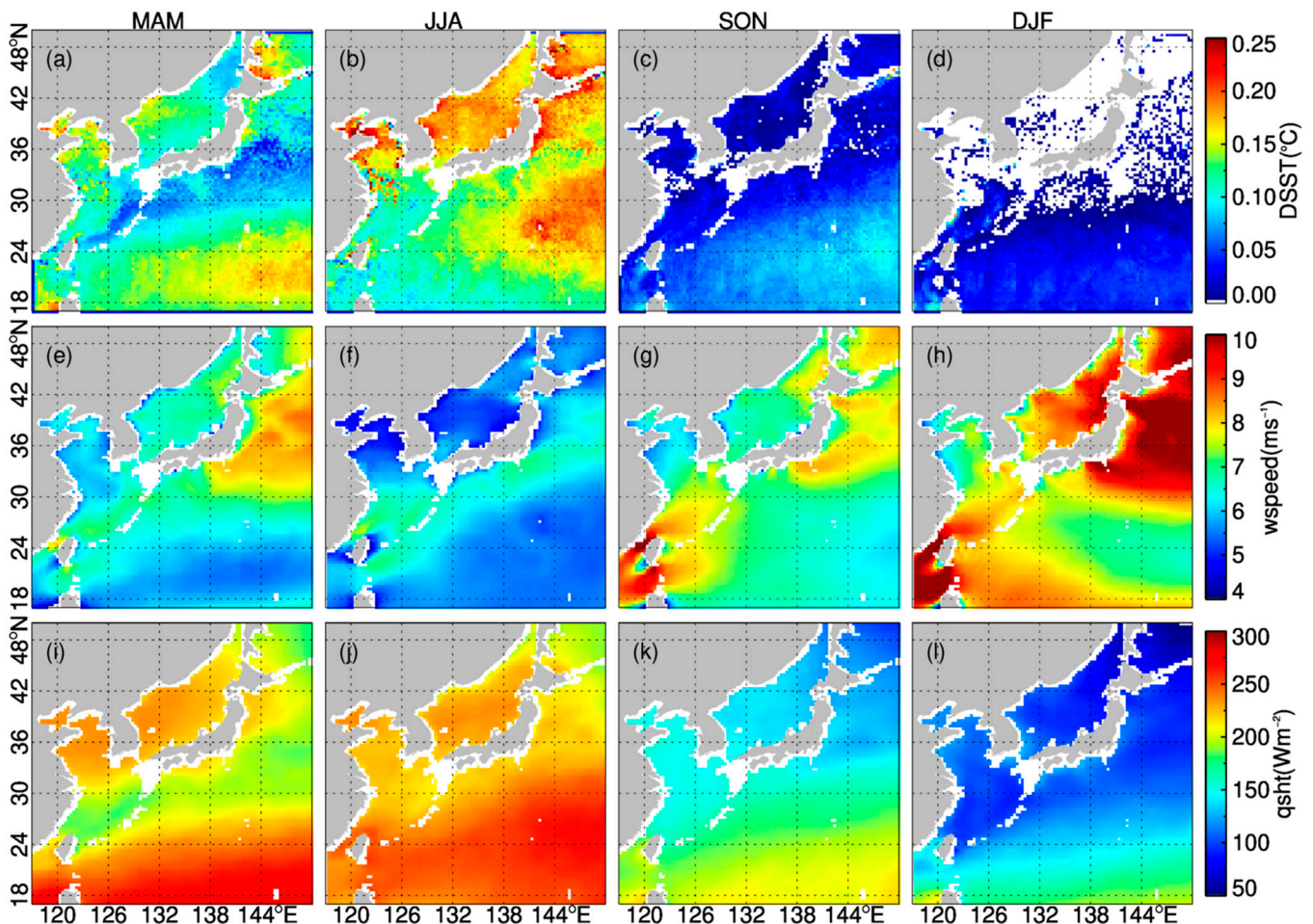


Figure 9. Seasonal variations in (a–d) SST DV; (e–h) wind speed and (i–l) shortwave radiation during the period 2019–2022.

To further discuss the relationship among the SST DV, shortwave radiation, and wind speed, we present the time series of these variables for the domain during this study period in Figure 10. To account for the different magnitude ranges of the variables, we normalize them as follows:

$$y = \frac{x - \bar{x}}{\bar{x}} \quad (7)$$

where x represents a variable, such as the difference between diurnal and non-diurnal SST and the corresponding calculated net heat flux, wind speed, and solar radiation, and \bar{x} is the average of the variable. As depicted in Figure 10, there is a clear positive correlation between SST DV and solar shortwave radiation. Positive SST DV only occurs when the normalized shortwave radiation is positive. In general, wind speed is negatively correlated with SST DV. Increased wind speeds reduce the surface heat flux and increase upper ocean mixing, which distributes surface heating to a greater depth of the ocean and reduces

surface warming. SST DV is responsible for the net heat flux variations. Slight variations in amplitude are found during the summer and winter seasons.

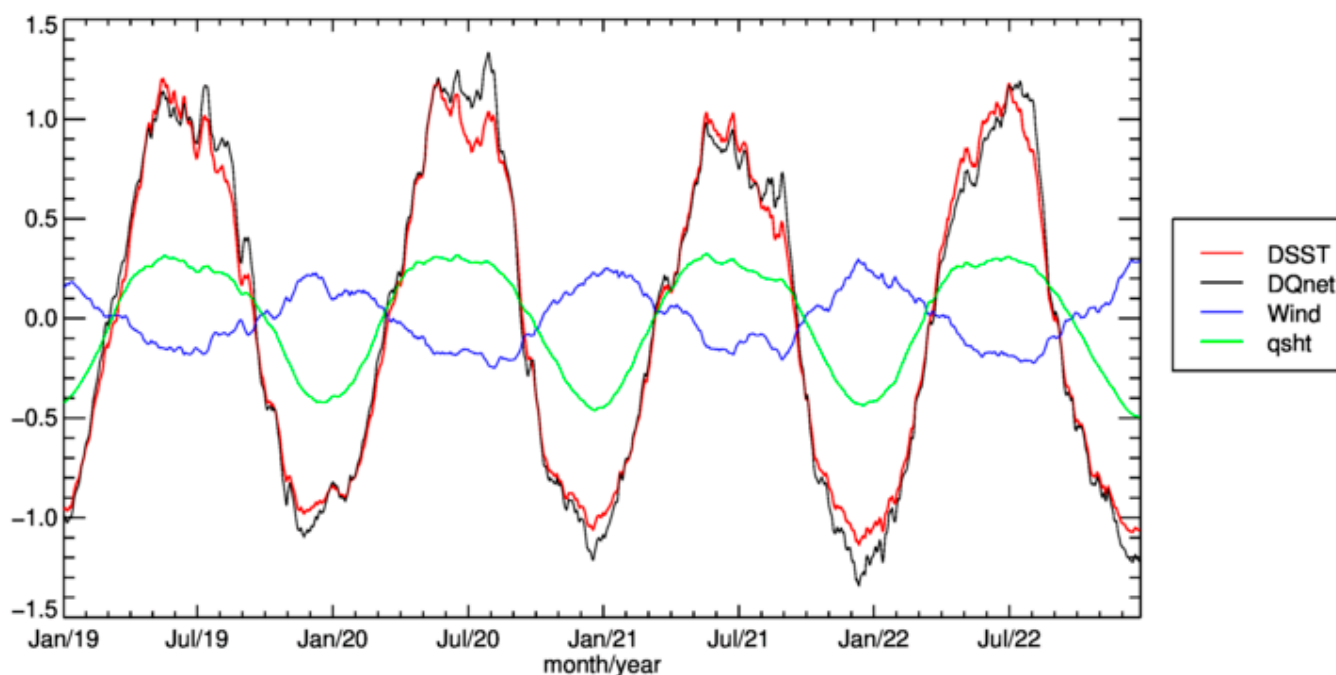


Figure 10. The normalization time series of daily average by a 45-day running mean for the difference between diurnal and non-diurnal SST (DSST) and the corresponding calculated net heat flux (DQnet), wind speed, and shortwave radiation (qsht) in domain-wide terms, respectively.

4.2. Implications

Differences in heat flux at the air–sea interface resulting from SST DV are widely observed. These differences are important for air–sea interactions and satellite remote sensing of sea surface conditions. They are also important for the initialization and diagnosis of oceanic and weather conditions. Furthermore, the understanding of energy and water cycle processes can be improved through this analysis.

To understand the complex dynamical processes of the upper ocean, it is useful to study the diurnal variability of the heat flux. Heat flux variability plays a crucial role in determining the vertical structure of the upper ocean. The heating and cooling cycles affect the stratification of the water column, resulting in temperature changes at different depths. SST DV creates spatial density gradients that contribute to the generation of baroclinic currents. These currents, in turn, influence wind-driven circulation patterns [35], forming a dynamic feedback loop between the ocean and the atmosphere. The layering process influenced by the diurnal heat flux has cascading effects on other oceanic phenomena. These effects include variations in the thermocline and the distribution of nutrients, which are integral to the overall health and productivity of marine ecosystems.

Studying the diurnal variation in heat flux is beneficial for understanding the water vapor circulation process. The water vapor budget is a vital component of the climate system, acting as the primary medium for the oceanic influence on atmospheric phenomena. Its role extends beyond local weather patterns, contributing to the broader atmospheric circulation that drives climate dynamics. Central to this process is the coupling of extreme latent heat to SST DV. When integrated into climate models, this coupling amplifies water vapor convection budgets. This has cascading effects on the strength and patterns of tropical seasonal oscillations, including the Madden–Julian Oscillation (MJO). The interplay of SST DV and extreme latent heat leads to enhanced water vapor convection budgets, which intricately shape the amplitude and frequency of MJO events. These findings have broad implications for understanding and predicting climate patterns. The representation of the

water vapor circulation, refined by accounting for diurnal heat flux variations, contributes to a more comprehensive understanding of how the oceans drive atmospheric convection on various temporal scales.

In addition, studying the diurnal variation in heat flux is helpful in understanding the global energy balance. The global air–sea energy exchange should approach equilibrium in the long term, maintaining a delicate balance. However, achieving this theoretical equilibrium has proven difficult due to challenges such as limited observational capability and inaccurate parameterization within flux estimation models. For flux applications on monthly to seasonal time scales, the accuracy requirement for Q_{net} is 10 W m^{-2} . The accuracy requirement is at least one order of magnitude higher, at $O(1 \text{ W m}^{-2})$ for Q_{net} , if the goal is to detect long-term trends against a background of natural variability [36]. The forcing field of flux models typically uses the daily mean SST without considering the diurnal variations. Therefore, further assessment is needed to determine their impact on the global energy balance.

5. Conclusions

This study provides insight into the complex dynamics of SST DV and its impact on heat fluxes at the air–sea interface over the NWPO. We compared SST DV data from ERA5 and JAXA-JAMSTEC using high-frequency observations from the KEO mooring buoy. The KEO measurements showed that the SST experienced a weak cooling during the nighttime from 00:00 to 06:00 LST, rising at 07:00 LST, plateauing 14:00 LST, and then gradually cooling. The SST DV has the highest amplitude in summer, followed by spring and autumn ($\sim 0.2\text{--}0.3 \text{ }^\circ\text{C}$), and is almost negligible in winter. Compared to the KEO observation, ERA5 showed a negative bias and a larger RMSE, while JAXA-JAMSTEC demonstrated excellent agreement with the KEO observations, with a very slight negative bias of $-0.007 \text{ }^\circ\text{C}$ and a RMSE of $0.018 \text{ }^\circ\text{C}$.

The importance of SST DV in shaping the spatial and temporal characteristics of heat fluxes was evident. The case study for 26 June 2020 illustrated the complex diurnal cycle, with warming amplitudes of up to $1.5 \text{ }^\circ\text{C}$ in the Yellow Sea, the northern ECS, and the subtropics. It is important to consider the SST DV in flux calculations to avoid substantial errors, especially in regions with significant diurnal warming. Significant differences of about $30\text{--}50 \text{ W m}^{-2}$ in net heat fluxes are observed over the ECS and SNWP in the early afternoon, highlighting the importance of including SST DV in heat flux calculations on daily time scales.

In addition, a thorough seasonal and temporal analysis revealed notable variations in heat flux when SST DV was either included or excluded. The average impact of SST DV on heat flux is 2.93 W m^{-2} over the subtropical NWPO and decreases from southeast to northwest and from low to high latitudes. Seasonal differences in SNWP are particularly pronounced, highlighting the role of solar radiation in driving these variations. Our results highlight the complex interactions among SST, solar radiation, and wind speed, and underscore the need for accurate representations in climate models for a nuanced understanding of air–sea interactions. This research provides valuable insights for both the oceanographic and meteorological communities. It emphasizes the need for careful consideration of high-temporal-resolution SST to resolve the diurnal cycle for robust climate and atmospheric studies.

Author Contributions: Conceptualization, Q.T. and Y.Y.; Data curation, D.L.; Formal analysis, Q.T.; Funding acquisition, Q.T., Z.H., B.T. and Y.Y.; Investigation, Q.T.; Methodology, Q.T.; Project administration, Z.H.; Resources, Z.H.; Software, L.S.; Supervision, Z.H.; Validation, B.T.; Visualization, D.L.; Writing—original draft, Q.T.; Writing—review and editing, Q.T. and Y.Y. All authors have read and agreed to the published version of the manuscript.

Funding: This work was supported in part by the National Key Research and Development Program of China (grant no. 2021YFC3101602 & 2022YFC3104203) and in part by the National Natural Science Foundation of China (grant no. 42006160 & 42376002).

Data Availability Statement: The hourly JAXA-JAMSTEC SST are available at https://www.eorc.jaxa.jp/ptree/ocean_model/index.html, accessed on 16 March 2023. The ERA5 hourly data are available at <https://cds.climate.copernicus.eu/cdsapp#!/dataset/reanalysis-era5-single-levels?tab=form>, accessed on 16 March 2023. The KEO data are available at <https://www.pmel.noaa.gov/ocs/data/disdel/>, accessed on 16 March 2023.

Acknowledgments: We thank the anonymous reviewers for their careful reading of our manuscript and their many insightful comments and suggestions.

Conflicts of Interest: The authors declare no conflicts of interest.

References

1. Cronin, M.F.; Gentemann, C.L.; Edson, J.; Ueki, I.; Bourassa, M.; Brown, S.; Clayson, C.A.; Fairall, C.W.; Farrar, J.T.; Gille, S.T.; et al. Air-Sea Fluxes with a Focus on Heat and Momentum. *Front. Mar. Sci.* **2019**, *6*, 430. [[CrossRef](#)]
2. Gentemann, C.L.; Clayson, C.A.; Brown, S.; Lee, T.; Parfitt, R.; Farrar, J.T.; Bourassa, M.; Minnett, P.J.; Seo, H.; Gille, S.T.; et al. FluxSat: Measuring the Ocean—Atmosphere Turbulent Exchange of Heat and Moisture from Space. *Remote Sens.* **2020**, *12*, 1796. [[CrossRef](#)]
3. Kawai, Y.; Wada, A. Diurnal sea surface temperature variation and its impact on the atmosphere and ocean: A review. *J. Oceanogr.* **2007**, *63*, 721–744. [[CrossRef](#)]
4. Sverdrup, H.U.; Johnson, M.W.; Fleming, R.H. *The Oceans: Their Physics, Chemistry, and General Biology*; Prentice-Hall: New York, NY, USA, 1942.
5. Stommel, H.; Saunders, K.; Simmons, W.; Cooper, J. Observations of the diurnal thermocline. *Deep Sea Res.* **1969**, *16*, 269–284.
6. Castro, S.L.; Wick, G.A.; Buck, J.J.H. Comparison of diurnal warming estimates from unpumped Argo data and SEVIRI satellite observations. *Remote Sens. Environ.* **2014**, *140*, 789–799. [[CrossRef](#)]
7. Karagali, I.; Høyer, J.L. Characterisation and quantification of regional diurnal SST cycles from SEVIRI. *Ocean Sci.* **2014**, *10*, 745–758. [[CrossRef](#)]
8. Stuart Menteth, A.C.; Robinson, I.S.; Challenor, P.G. A global study of diurnal warming using satellite-derived sea surface temperature. *J. Geophys. Res. Ocean.* **2003**, *108*, C5. [[CrossRef](#)]
9. Tu, Q.; Pan, D.; Hao, Z.; Yan, Y. SST diurnal warming in the China seas and northwestern Pacific Ocean using MTSAT satellite observations. *Acta Oceanol. Sin.* **2016**, *35*, 12–18. [[CrossRef](#)]
10. Yan, Y.; Zhang, L.; Song, X.; Wang, G.; Chen, C. Diurnal variation in surface latent heat flux and the effect of diurnal variability on the climatological latent heat flux over the tropical oceans. *J. Phys. Oceanogr.* **2021**, *51*, 3401–3415. [[CrossRef](#)]
11. Webster, P.J.; Clayson, C.A.; Curry, J.A. Clouds, Radiation, and the Diurnal Cycle of Sea Surface Temperature in the Tropical Western Pacific. *J. Clim.* **1996**, *9*, 1712–1730. [[CrossRef](#)]
12. Fairall, C.W.; Bradley, E.F.; Godfrey, J.S.; Wick, G.A.; Edson, J.B.; Young, G.S. Cool-skin and warm-layer effects on sea surface temperature. *J. Geophys. Res.* **1996**, *101*, 1295–1308. [[CrossRef](#)]
13. Parsons, D.B.; Redelsperger, J.; Yoneyama, K. The evolution of the tropical western Pacific atmosphere-ocean system following the arrival of a dry intrusion. *Q. J. R. Meteorol. Soc.* **2000**, *126*, 517–548.
14. Zeng, X.; Dickinson, R.E. Impact of diurnally-varying skin temperature on surface fluxes over the tropical Pacific. *Geophys. Res. Lett.* **1998**, *25*, 1411–1414. [[CrossRef](#)]
15. Ward, B. Near-surface ocean temperature. *J. Geophys. Res. Ocean.* **2006**, *111*, C2. [[CrossRef](#)]
16. Clayson, C.A.; Bogdanoff, A.S. The Effect of Diurnal Sea Surface Temperature Warming on Climatological Air-Sea Fluxes. *J. Clim.* **2013**, *26*, 2546–2556. [[CrossRef](#)]
17. Yan, Y.; Song, X.; Wang, G.; Li, X. Tropical Cool-skin and Warm-layer Effects and their Impact on Surface Heat Fluxes. *J. Phys. Oceanogr.* **2024**, *54*, 45–62. [[CrossRef](#)]
18. Moltmann, T.; Turton, J.; Zhang, H.; Nolan, G.; Gouldman, C.; Griesbauer, L.; Willis, Z.; Piniella, Á.M.; Barrell, S.; Andersson, E.; et al. A Global Ocean Observing System (GOOS), Delivered Through Enhanced Collaboration Across Regions, Communities, and New Technologies. *Front. Mar. Sci.* **2019**, *6*, 291. [[CrossRef](#)]
19. Lin, J.; Wang, Y.; Pan, H.; Wei, Z.; Xu, T. Uncertainty of CYGNSS-Derived Heat Flux Variations at Diurnal to Seasonal Time Scales over the Tropical Oceans. *Remote Sens.* **2023**, *15*, 3161. [[CrossRef](#)]
20. Soloviev, A.; Lukas, R. *The Near-Surface Layer of the Ocean: Structure, Dynamics and Applications*; Springer Science & Business Media: Berlin/Heidelberg, Germany, 2013.
21. Marullo, S.; Minnett, P.J.; Santoleri, R.; Tonani, M. The diurnal cycle of sea-surface temperature and estimation of the heat budget of the Mediterranean Sea. *J. Geophys. Res. Ocean.* **2016**, *121*, 8351–8367. [[CrossRef](#)]
22. Wang, H.; Liu, D.; Zhang, W.; Li, J.; Wang, B. Characterizing the capability of mesoscale eddies to carry drifters in the northwest Pacific. *J. Oceanol. Limnol.* **2020**, *38*, 1711–1728. [[CrossRef](#)]
23. Kurihara, Y.; Murakami, H.; Kachi, M. Sea surface temperature from the new Japanese geostationary meteorological Himawari-8 satellite. *Geophys. Res. Lett.* **2016**, *43*, 1234–1240. [[CrossRef](#)]

24. Kurihara, Y.; Murakami, H.; Ogata, K.; Kachi, M. A quasi-physical sea surface temperature method for the split-window data from the Second-generation Global Imager (SGLI) onboard the Global Change Observation Mission-Climate (GCOM-C) satellite. *Remote Sens. Environ.* **2021**, *257*, 112347. [[CrossRef](#)]
25. Shibata, A.; Imaoka, K.; Koike, T. AMSR/AMSR-E level 2 and 3 algorithm developments and data validation plans of NASDA. *IEEE Trans. Geosci. Remote Sens.* **2003**, *41*, 195–203. [[CrossRef](#)]
26. Miyazawa, Y.; Varlamov, S.M.; Miyama, T.; Guo, X.; Hihara, T.; Kiyomatsu, K.; Kachi, M.; Kurihara, Y.; Murakami, H. Assimilation of high-resolution sea surface temperature data into an operational nowcast/forecast system around Japan using a multi-scale three-dimensional variational scheme. *Ocean Dyn.* **2017**, *67*, 713–728. [[CrossRef](#)]
27. Hersbach, H.; Bell, B.; Berrisford, P.; Biavati, G.; Horányi, A.; Muñoz Sabater, J.; Nicolas, J.; Peubey, C.; Radu, R.; Rozum, I.; et al. ERA5 Hourly Data on Single Levels from 1940 to Present. Copernicus Climate Change Service (C3S) Climate Data Store (CDS). 2023. Available online: <https://cds.climate.copernicus.eu/cdsapp#!/dataset/reanalysis-era5-single-levels?tab=overview> (accessed on 15 December 2023).
28. Cronin, M.F.; Weller, R.A.; Lampitt, R.S.; Send, U. Ocean reference stations. In *Earth Observation*; Elsevier: Amsterdam, The Netherlands, 2012; pp. 203–228.
29. Fairall, C.W.; Bradley, E.F.; Hare, J.E.; Grachev, A.A.; Edson, J.B. Bulk parameterization of air–sea fluxes: Updates and verification for the COARE algorithm. *J. Clim.* **2003**, *16*, 571–591. [[CrossRef](#)]
30. Hsu, C.W.; DeMott, C.A.; Branson, M.D.; Reeves Eyre, J.; Zeng, X. Ocean Surface Flux Algorithm Effects on Tropical Indo-Pacific Intraseasonal Precipitation. *Geophys. Res. Lett.* **2022**, *49*, e2021GL096968. [[CrossRef](#)] [[PubMed](#)]
31. Brunke, M.A.; Fairall, C.W.; Zeng, X.; Eymard, L.; Curry, J.A. Which bulk aerodynamic algorithms are least problematic in computing ocean surface turbulent fluxes? *J. Clim.* **2003**, *16*, 619–635. [[CrossRef](#)]
32. Edson, J.B.; Jampana, V.; Weller, R.A.; Bigorre, S.P.; Plueddemann, A.J.; Fairall, C.W.; Miller, S.D.; Mahrt, L.; Vickers, D.; Hersbach, H. On the Exchange of Momentum over the Open Ocean. *J. Phys. Oceanogr.* **2013**, *43*, 1589–1610. [[CrossRef](#)]
33. Yan, Y.; Wang, G.; Wang, X.H.; Chen, C.; Ling, Z.; Zhang, L. Relationship between subsurface diurnal warming and wind speed. *Deep. Sea Res. Part I Oceanogr. Res. Pap.* **2023**, *199*, 104106. [[CrossRef](#)]
34. Yang, Y.; Li, K.; Yu, W.; Zu, Y.; Liu, L. Modulation of observed sea surface temperature variation by the quasi-biweekly oscillation in the tropical western Pacific during boreal summer. *Int. J. Climatol.* **2022**, *42*, 3173–3189. [[CrossRef](#)]
35. Ide, Y.; Yoshikawa, Y. Effects of diurnal cycle of surface heat flux on wind-driven flow. *J. Oceanogr.* **2016**, *72*, 263–280. [[CrossRef](#)]
36. Yu, L. Global Air-Sea Fluxes of Heat, Fresh Water, and Momentum: Energy Budget Closure and Unanswered Questions. *Annu. Rev. Mar. Sci.* **2019**, *11*, 227–248. [[CrossRef](#)] [[PubMed](#)]

Disclaimer/Publisher’s Note: The statements, opinions and data contained in all publications are solely those of the individual author(s) and contributor(s) and not of MDPI and/or the editor(s). MDPI and/or the editor(s) disclaim responsibility for any injury to people or property resulting from any ideas, methods, instructions or products referred to in the content.